THE JOURNAL OF PHYSICAL CHEMISTRY C

Article

pubs.acs.org/JPCC

Electron Beam Induced Reactions of Adsorbed Cobalt Tricarbonyl Nitrosyl ($Co(CO)_3NO$) Molecules

Samantha G. Rosenberg, Michael Barclay, and D. Howard Fairbrother*

Department of Chemistry, Johns Hopkins University, Baltimore, Maryland 21218, United States

Supporting Information

ABSTRACT: This study focuses on elucidating the bond breaking steps involved in the electron beam induced deposition (EBID) of nanostructures created from the organometallic precursor cobalt tricarbonyl nitrosyl ($Co(CO)_3NO$) by studying the effect of 500 eV incident electrons on nanometer scale films of $Co(CO)_3NO$. Experiments were performed under ultrahigh vacuum conditions, using a suite of surface analytical techniques, principally X-ray photoelectron spectroscopy and mass spectrometry. The purely electron stimulated reactions of $Co(CO)_3NO$ adsorbed on gold or amorphous carbon substrates at low temperatures (−168 °C) occurs in two distinct steps. The first step involves a one electron process that initiates decomposition of the nitrosyl (NO) ligand to form a nitride, accompanied by the simultaneous desorption of at least one CO ligand to create a partially decarbonylated intermediate. This first step decomposes $Co(CO)_3NO$ into a nonvolatile Co-containing compound and therefore initiates the EBID process. In the second step, the residual CO ligands in the partially decarbonylated fragments undergo electron stimulated decomposition as opposed to desorption, leading to the formation of adsorbed carbon and oxidized cobalt atoms. However, carbon atoms in the partially decarbonylated species formed during the first step are thermally labile below room temperature. This provides a rationale for the observation that EBID nanostructures created from $Co(CO)_3NO$ under steady state deposition conditions, at ambient temperatures, typically contain very low levels of carbon contamination. Results from this study highlight the importance that both electron and thermally stimulated processes can play in determining the ultimate chemical composition of nanostructures created by EBID.

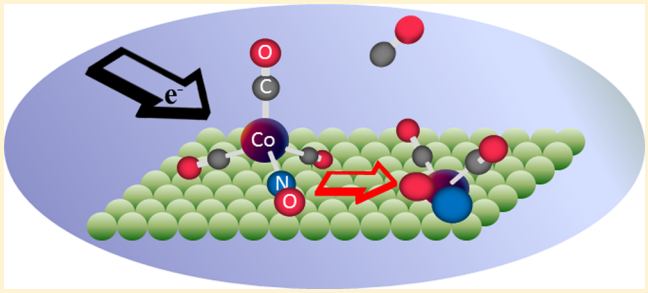

INTRODUCTION

One of the most versatile means of fabricating and prototyping metal-containing nanostructures is electron beam induced deposition (EBID), also known as focused electron beam induced processing (FEBIP). EBID is a vacuum based process that uses focused electron beams to decompose transiently adsorbed organometallic precursor molecules into nanosized structures in a single-step, without the need for resists or solvents.[1−4] Other advantages of EBID include the flexibility to deposit an almost limitless array of free-standing, 3D, nanometer scale structures without the often negative effects of ion beam deposition techniques (e.g., Ga implantation). The increasing importance of EBID as a tool for manipulating and controlling nanoscale devices can be seen in the rapid increase in the number of published articles over the past decade[5−11] and the appearance of several recent review articles.[1−3,5]

The choice of organometallic precursor for a particular EBID application is usually dictated by the chemical and/or physical property requirements for the central metal atom and the experimental need for the precursor to be suitably volatile, nontoxic, and commercially available. For example, trimethyl-(methylcyclopentadienyl)platinum(IV) ($MeCpPtMe_3$) is often chosen for nanoelectronic applications and the creation of nanowires due to the conductive properties of the central platinum atom.[4,12−15] Cobalt-containing organometallic precursors are often selected for EBID applications where nanostructures are being fabricated for ferromagnetic and/or catalytic applications. Thus, cobalt EBID nanostructures have been used to fabricate magnetic force microscopy tips,[16,17] cross bar hall sensors,[7] ferromagnetic nanowires[18,19] and to create catalytic nanoparticles for carbon nanotube synthesis.[20] In a recent study, Gazzadi et al, have shown that cobalt nanowires made by EBID and annealed to 400 °C under vacuum exhibit a metallic-like resistivity (ρ = 62 $\mu\Omega$ cm at RT) and magnetic behavior.[19] The two most widely used cobalt-containing precursors in EBID are cobalt octacarbonyl, $Co_2(CO)_8$, and cobalt tricarbonyl nitrosyl, $Co(CO)_3NO$.[16,17,21,22] Cobalt tricarbonyl nitrosyl is particularly appealing as an EBID precursor due to its relative ease of use (e.g., nontoxicity) and desirable physical properties (e.g., volatility). For these reasons, $Co(CO)_3NO$ has also been used in chemical vapor deposition (CVD) as a precursor for the deposition of pure cobalt films at substrate temperatures >250 °C.[23−26]

Received: May 18, 2013
Revised: June 28, 2013
Published: July 1, 2013

   dx.doi.org/10.1021/jp404905t | J. Phys. Chem. C 2013, 117, 16053−16064

Although there are many benefits of EBID, one main drawback is the often low metal content in the deposits due to an undesirably high level of organic contamination (particularly carbon) that is codeposited along with the metal.[13,14,27,28] This contamination adversely affects the properties of many EBID deposits, such as conductivity and catalytic activity, and emanates from two sources: gases present in the low vacuum environment of the electron microscope (most notably hydrocarbons) and from decomposition of the ligands associated with the organometallic precursor. The metal content of EBID nanostructures created using $MeCpPtMe_3$, one of the most popular precursors, is frequently less than 20%,[2,13−15,29] and many other EBID precursors produce nanostructures with similarly poor metallic content.[30−32] In contrast, EBID deposits created with $Co(CO)_3NO$ have been reported to have approximately 50% Co content on average and carbon levels on the order of 10%.[18,19,29] These different characteristics compared to most other EBID precursors suggests that a more detailed, molecular level, understanding of how $Co(CO)_3NO$ molecules react and transform during the EBID process may help in the design of new precursors that yield nanostructures with higher metal content. Indeed, as pointed out by Mulders et al., 100% metal purity is not always necessary as long as the local structure satisfies the requirements of the particular application.[29]

As an important step in developing a more detailed fundamental understanding of how $Co(CO)_3NO$ reacts during the EBID process, Engmann et al., have recently determined the absolute cross sections and branching ratios for the reactions of gas phase $Co(CO)_3NO$ with low energy electrons (1−140 eV).[33,34] Motivation for these studies derives from the fact that large numbers of low energy secondary electrons are produced during the EBID process as a result of interactions between the high energy primary beam and the substrate. These species are often cited as being responsible for initiating the deposition process, as well as a broadening of feature sizes in deposited nanostructures.[2,35] Results from these gas phase studies indicate that dissociative electron attachment (DEA) to $Co(CO)_3NO$ by low energy electrons (<10 eV) lead predominantly to the loss of a single CO ligand, while higher energy electron interactions (>70 eV) lead to dissociative ionization (DI) and produce bare Co atoms as the dominant product.[33,34]

In the present study, we have used a number of ultrahigh vacuum (UHV), surface science techniques to follow the electron stimulated reactions of cobalt tricarbonyl nitrosyl ($Co(CO)_3NO$) adsorbed at low temperatures onto Au or amorphous carbon (a:C) substrates. These surface science studies represent an increasing level of complexity compared to gas phase studies but have a greater relevance to the EBID process. Compared to studies conducted in electron microscopes, the low temperature-UHV approach facilitates the acquisition of molecular level information on EBID. The low pressure conditions eliminate contributions from impurity gases while the low substrate temperatures enable us to create and follow the electron stimulated reactions of a well-defined adsorbate layer in situ, including the identification of volatile gas phase species produced by electron irradiation. To enable the use of surface analytical techniques such as X-ray photoelectron spectroscopy (XPS), that are ill equipped to interrogate nanostructures, we create adsorbate layers on ∼1 cm^2 substrates and use a low energy (500 eV) flood gun to generate a relatively broad and defocused electron beam that exhibits a roughly uniform flux over the sample surface. This approach has already proved effective in elucidating the electron stimulated decomposition mechanism of several other EBID precursors, $MeCpPtMe_3$,[36] $Au(acac)Me_2$,[37] $Pt(PF_3)_4$,[38] and $W(CO)_6$.[39] In general we have found that electron stimulated reactions of organometallic precursors react in two discrete phases: the initial deposition step characterized by ligand desorption, and the second step, driven by electron stimulated decomposition of the remaining ligands.[38,39] Recently, we have also recognized that the fate of intermediates produced in the initial deposition step by electron irradiation can be influenced by the substrate's temperature.[40] Motivated by these findings we have included annealing experiments in the present study to probe the fate of intermediates produced during electron irradiation.

EXPERIMENTAL SECTION

Three separate UHV chambers were used. Most experiments were performed in an UHV chamber equipped with XPS and MS. A second UHV chamber was equipped with reflective absorption infrared spectrometry (RAIRS). These two chambers were used to study the effect of electron irradiation on nanometer thick films of $Co(CO)_3NO$ adsorbed onto Au or (a:C) substrates. The third chamber was a scanning Auger electron spectroscopy (AES) system that was used to deposit and monitor the chemical composition of films grown from $Co(CO)_3NO$ under more typical EBID conditions (i.e., steady state deposition with the substrate at ambient temperature). All three of the UHV chambers ($P_{base} < 5 \times 10^{-9}$ Torr for the XPS/MS and AES system; $P_{base} \approx 2 \times 10^{-8}$ Torr for the RAIRS system) and their capabilities have been described previously.[36−40] Brief descriptions of the various experimental elements are provided in the following sections.

Precursor. Cobalt tricarbonyl nitrosyl ($Co(CO)_3NO$; CAS 14096-82-3, Strem Chemicals, Inc.) is a dark red liquid at standard temperature and pressure (STP). The precursor was attached to a stainless steel gas manifold, which was coupled to each UHV chamber via a leak valve. The gas manifold was evacuated and the precursor purified by several freeze-pump thaw cycles. The gas manifold was then filled with a partial pressure of the precursor by placing the $Co(CO)_3NO$ into an ice bath while heating the surrounding gas manifold to ∼25 °C.

Substrates. Most MS and XPS experiments were conducted on a polycrystalline Au substrate, with a few comparative experiments conducted on an (a:C) substrate. For all RAIRS experiments a polished Au mirror was used as the substrate. Polycrystalline Au was chosen for XPS, MS, and RAIRS experiments because of its relative ease of cleaning, lack of spectral overlap with any of the prominent Co, C, N, or O XPS transitions, reflectivity (when polished), and general lack of reactivity. Substrates were mounted onto a manipulator with the capability for *xyz* translation and rotation as well as the ability to be liquid-nitrogen-cooled and resistively heated. In the chamber with XPS and MS the polycrystalline Au substrate was regenerated by ion sputtering with 4 keV Ar^+ (>1 h). In RAIRS experiments the polycrystalline Au was polished to increase reflectivity but could not be cleaned in vacuum. In the AES chamber, EBID was performed on a sputter cleaned (a:C) substrate at ambient temperatures.

Creating Films. In the XPS/MS and RAIRS chambers films were created by leaking $Co(CO)_3NO$ into the chamber through an UHV compatible leak valve and onto a cooled (−168 °C) Au or (a:C) substrate. The film thickness was

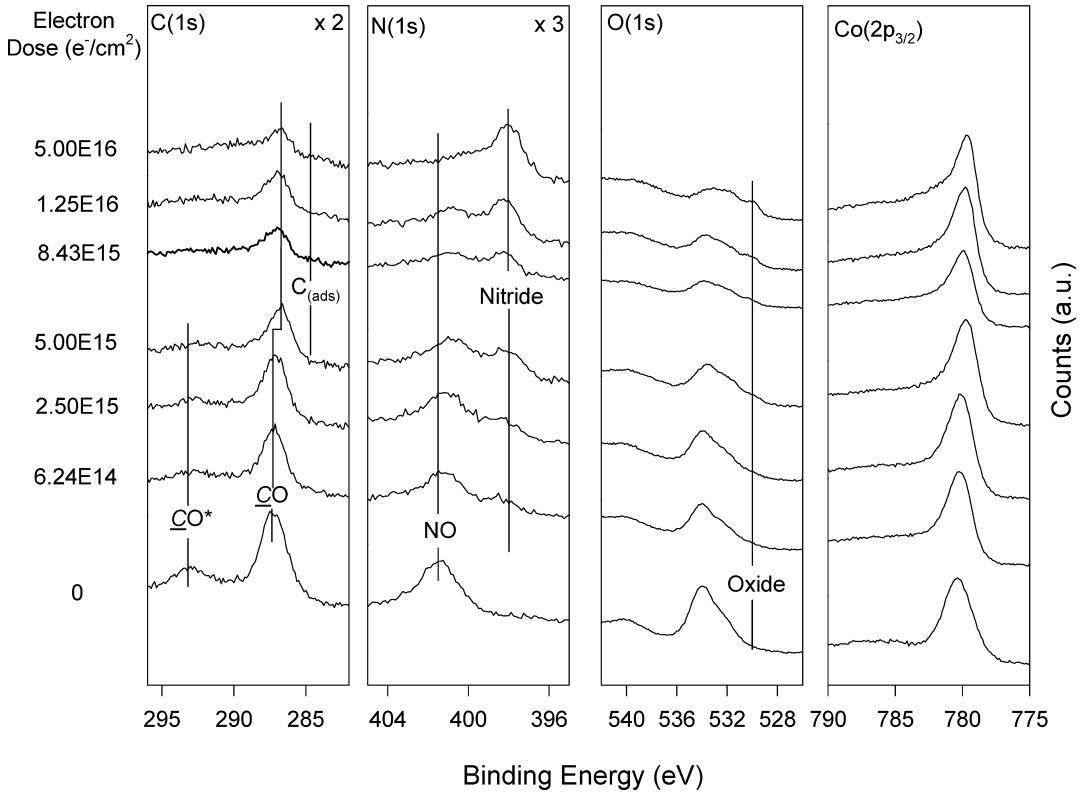

Figure 1. Evolution of the C(1s), N(1s), O(1s), and Co($2p_{3/2}$) XP regions for 2.3−2.5 nm thick films of $Co(CO)_3NO$ exposed to electron doses $<5.00 \times 10^{16}$ e^-/cm^2. Films were adsorbed onto a gold substrate at −168 °C, and the incident electron energy was 500 eV. The corresponding electron dose is shown on the left-hand side of each set of spectra.

determined by measuring the signal attenuation from the substrate's photoelectrons by XPS. For Au(4f) and C(1s) photoelectrons an inelastic mean free path of 2.0 nm was used.[41] Based on the physical properties of liquid phase $Co(CO)_3NO$, film thicknesses used in this study corresponded to average coverages of ∼8−10 monolayers. In RAIRS experiments, film thicknesses were not determined quantitatively and were measured in terms of the nominal $Co(CO)_3NO$ exposure as recorded by a nude ion gauge.

In the AES system, films were created by leaking $Co(CO)_3NO$ into the chamber through an UHV compatible leak valve coupled to a directional doser to create a constant partial pressure of $Co(CO)_3NO$ during deposition. While dosing, the electron beam was rastered across the surface to produce rectangular structures. The films were made with a current of 4.4 μA and a partial pressure of 2.00×10^{-7} Torr. Deposition times ranged from 120 to 480 s.

Electron Sources. In the XPS/MS chamber, once the film's thickness and composition were determined, it was exposed to a known electron dose using a commercial flood gun (Specs FG 15/40) that served as a broad beam electron source. For RAIRS experiments, a home-built electron gun, previously described, was used as a broad beam electron source.[39] For both electron sources, the beam characteristics were characterized using a previously described procedure.[36,39,40] Both sources were thoroughly outgassed prior to use, to avoid the deposition of adventitious hydrocarbons or other species during experiments. An incident electron energy of 500 eV was used throughout XPS, MS, and RAIRS experiments, calculated from the sum of the electron energy generated by the flood gun (480 eV) and a positive bias (+20 V) applied to the substrate to attract secondary electrons emitted during irradiation. The target current was held at 5 μA, unless otherwise noted, as determined by a picoammeter connected to the substrate through the heating rods. For all XPS and MS experiments, electron irradiation was reported in terms of dose (e^-/cm^2). For RAIRS experiments, electron dose was reported in terms of irradiation time due to uncertainties in the nature of the surface and the thickness of the adsorbate layer. For all AES experiments, the electrons were created with a LaB_6 filament and rastered to produce two structure sizes: a 600 μm × 429 μm deposit and a 300 μm × 214 μm deposit.

Analytical Techniques. *X-ray Photoelectron Spectroscopy.* XPS was performed using Mg Kα X-rays ($h\nu$ = 1253.6 eV) and spectra were deconvoluted with commercial software (CASA XPS). Peak positions obtained for $Co(CO)_3NO$ films deposited on Au substrates were aligned to the Au($4f_{7/2}$) peak at 84 eV, while films deposited on (a:C) substrates were aligned to the C(1s) peak at 284.6 eV.[42] All XP spectra were recorded with a step size of 0.125 eV and at pass energies of 22 eV.

Mass Spectrometry. A quadrupole mass spectrometer (QMS, Stanford Research System, 0−200 amu) was used to monitor neutral gas phase products produced during electron irradiation and the purity of the gas in the dosing line. The QMS was positioned ∼10 cm from the substrate and in a direct line-of-sight.

Auger Electron Spectrometry. In AES experiments, the film's chemical composition was characterized using 3 keV electrons.

Reflection Absorption Infrared Spectroscopy. RAIR spectra were obtained with a Mattson Infinity Series FTIR by passing an IR beam through differentially pumped ZnSe windows.

dx.doi.org/10.1021/jp404905t | J. Phys. Chem. C 2013, 117, 16053−16064

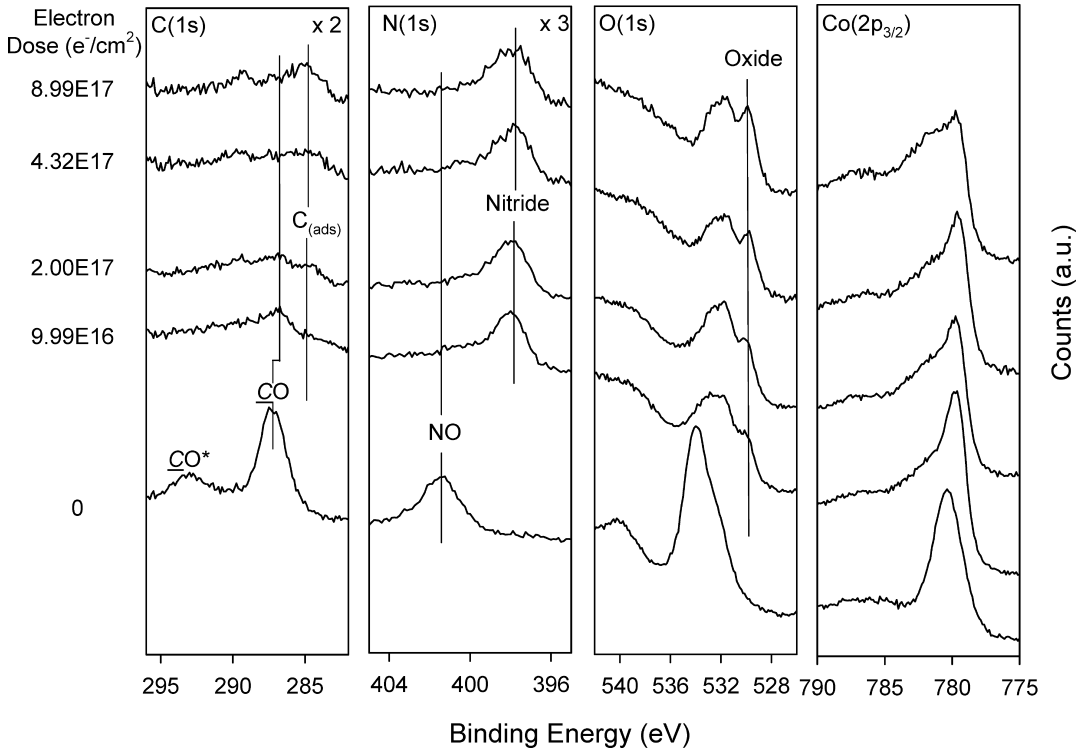

Figure 2. Evolution of the C(1s), N(1s), O(1s), and $Co(2p_{3/2})$ XP regions for 2.3−2.5 nm thick films of $Co(CO)_3NO$ exposed to electron doses >5.00 × 10^{16} e^-/cm^2. For reference, the lowest spectra is a film prior to electron irradiation (electron dose = 0 e^-/cm^2). Films were adsorbed onto a gold substrate at −168 °C and the incident electron energy was 500 eV. The corresponding electron dose is shown on the left-hand side of each set of spectra.

Spectra were recorded with a narrow band MCT detector (400−4000 cm^{-1}), operating at a resolution of 4 cm^{-1}.

RESULTS

Figures 1 and 2 show the evolution in the C(1s), N(1s), O(1s), and $Co(2p_{3/2})$ regions measured by XPS for 2.3−2.5 nm thick $Co(CO)_3NO$ films as a function of increasing electron dose. The sensitivity of the adlayer to the effects of secondary electrons produced by the X-rays was determined in separate control studies, shown in Figure S1. Results from these studies, conducted for 280 min of total X-ray exposure, revealed that over this time period X-ray irradiation induced changes in the C(1s) and N(1s) regions. Due to this sensitivity, XPS analysis was conducted only on the deposited film and then again after a single electron dose. Collectively this analysis time corresponds to a total of 80 min X-ray exposure. Thus, the XPS data shown in Figure 1 and 2 represents multiple experiments performed on different $Co(CO)_3NO$ films that exhibited comparable initial thicknesses, but which were exposed to different electron doses.

Figure 1 focuses on the effects that comparatively small electron doses (≤5 × 10^{16} e^-/cm^2) have on adsorbed $Co(CO)_3NO$ molecules. Prior to electron irradiation the C(1s) region consists of two peaks, centered at 287.8 and 293.3 eV. The lower binding energy peak can be ascribed to the C(1s) peak of CO ligands in $Co(CO)_3NO$, while the higher binding energy peak is a shake up feature, associated with a $\pi-\pi^*$ transition that can accompany the excitation of a C(1s) core level electron in a metal carbonyl.[43,44] Figure 1 shows that changes in the C(1s) region, due to electron doses ≤5 × 10^{16} e^-/cm^2, are characterized by decreases in intensity of both C(1s) peaks in the absence of any new spectral features. The N(1s) region is initially composed of one peak centered at 401.6 eV, indicative of NO ligands.[44] The NO shake up feature, expected at 408.4 eV,[44] could not be resolved due to an overlap with satellite peaks from the Au substrate. As a function of increasing electron dose, the intensity of the NO peak decreases systematically, but its loss is accompanied by the appearance of a new peak centered at 398.1 eV. Based on literature values this new feature, shifted to lower binding energy by 3.5 eV compared to the NO species, is assigned to a nitride species.[45,46] The nitride peak continues to grow in intensity with increasing electron dose until it is the only feature remaining in the N(1s) region for electron doses ≥5 × 10^{16} e^-/cm^2. Before electron irradiation, the O(1s) region exhibits two peaks. The largest peak, centered at 534.0 eV, has contributions from both the CO and NO ligands that are too close to be resolved (534.0 eV for CO, and 534.6 eV for NO),[44] producing a single asymmetric peak. The second, smaller peak in the O(1s) region, centered at 540.0 eV is a $\pi-\pi^*$ shake up feature, typically observed in XPS for both CO and NO ligands.[43,44] For electron doses ≤5 × 10^{16} e^-/cm^2, changes in the O(1s) region shown in Figure 1 are dominated by a loss of intensity for all peaks, accompanied by the appearance of a small contribution from a third peak, centered at 529.7 eV, ascribed to an oxide.[47−49] Prior to electron irradiation the $Co(2p_{3/2})$ region initially consists of one peak, centered at 780.9 eV, consistent with previous reported values for molecular $Co(CO)_3NO$.[44] For comparatively small electron doses (≤5 × 10^{16} e^-/cm^2), Figure 1 shows that the only change is a subtle broadening to higher binding energies. Analysis of the integrated area within the $Co(2p_{3/2})$ region reveals that no Co atoms are lost from the surface as a result of electron

dx.doi.org/10.1021/jp404905t | J. Phys. Chem. C 2013, 117, 16053−16064

exposure. In other words there is no electron stimulated $Co(CO)_3NO$ desorption.

Figure 2 shows the effect of electron doses in excess of 5×10^{16} e^-/cm^2. In the C(1s) region, the peaks associated with CO continue to decrease but this is now accompanied by the appearance of a new peak, centered at 285 eV, whose peak position can be ascribed to graphitic carbon (C_{ads}).[42] The intensity of the C_{ads} peak continues to grow as the electron dose increases for values $>5 \times 10^{16}$ e^-/cm^2. There are essentially no changes in the N(1s) region for electron doses in excess of 5×10^{16} e^-/cm^2, while in the O(1s) region the peaks observed prior to electron irradiation continue to decrease in intensity, while the oxide peak centered at 529.7 eV becomes more intense. It should be noted that although oxides of cobalt produce peaks over a range of binding energies (529.50−532.3 eV),[47−49] we have chosen to use the lowest binding energy feature at 529.7 eV because it does not overlap with the peak positions of CO or NO ligands[44] and can therefore be unambiguously assigned. For electron doses, $> 5 \times 10^{16}$ e^-/cm^2, the largest spectral changes actually occur in the $Co(2p_{3/2})$ region, with a pronounced increase in the broadening to higher binding energies due to the production of oxidized cobalt atoms. For electron doses greater than 8.99×10^{17} e^-/cm^2, the C(1s), N(1s), O(1s), and $Co(2p_{3/2})$ regions no longer change in intensity or spectral profile (shape, peak position).

It is worth noting that the effect of 500 eV electrons mirrors that of X-ray irradiation. Thus, a comparison of Figures 1, 2, and Figure S1 reveal that the C(1s), N(1s), O(1s), and $Co(2p_{3/2})$ regions observed after an electron dose of 5.00×10^{15} e^-/cm^2 are comparable to those observed in Figure S1 for a $Co(CO)_3NO$ film exposed to 240 min of total X-ray irradiation time.

Figure 3 shows the variation in the integrated spectral intensity within the C(1s), N(1s), and O(1s) regions as a function of electron dose. Each data point represents the integrated XPS area for an element after irradiation, normalized to the value measured for the $Co(CO)_3NO$ film before electron exposure. Qualitatively, the C/C_0 and O/O_0 ratios exhibit similar variations, decreasing significantly to ~40−50% of their initial values for electron doses $\leq 5 \times 10^{16}$ e^-/cm^2, but remains relatively constant thereafter. In contrast, the N/N_0 ratio remains relatively constant for all electron doses.

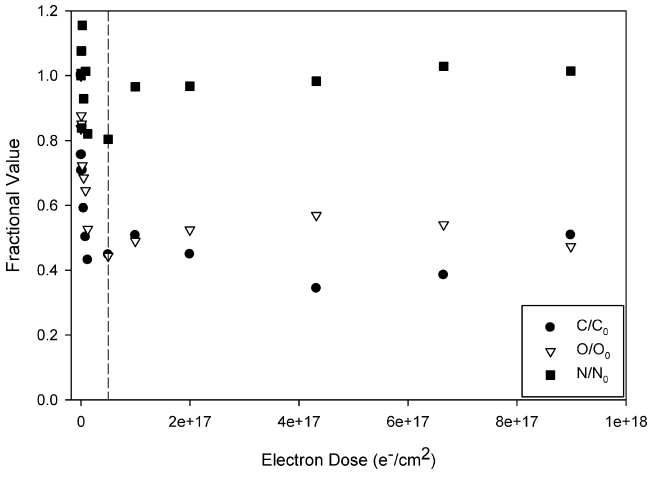

Figure 3. Change in the fractional coverage of adsorbed carbon, oxygen, and nitrogen atoms for 2.3−2.5 nm $Co(CO)_3NO$ films, plotted as a function of electron dose. Each relative concentration (C/C_0, O/O_0, and N/N_0) was determined by XPS. The initial C_0, O_0, and N_0 values were measured prior to electron irradiation. Films were adsorbed onto Au at −168 °C and exposed to 500 eV electrons. The vertical dotted line represents an electron dose of 5.00×10^{16} e^-/cm^2.

In Figure 4 the variation in the fractional coverage of NO species (NO/NO_0), observed at 401.6 eV in Figure 1, and graphitic carbon (C_{ads}), observed at 285 eV in Figure 2, are plotted as a function of electron dose on a logarithmic scale. For electron doses $\leq 5 \times 10^{16}$ e^-/cm^2, Figure 4 shows that the concentration of adsorbed NO species decreases while there is no measurable production of C_{ads}. Once an electron dose ~5×10^{16} e^-/cm^2 has been reached, all of the NO_0 species have been depleted. This electron dose also closely corresponds to the onset of C_{ads} production.

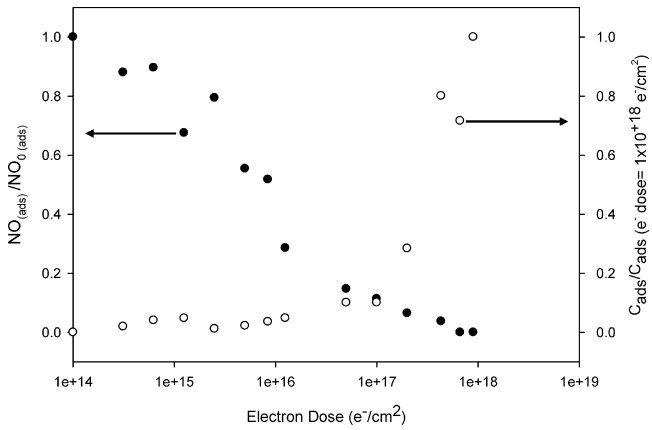

Figure 4. Change in the fractional concentration of graphitic carbon (C_{ads}, open circles) and NO species (filled circles) for 2.3−2.5 nm $Co(CO)_3NO$ films, plotted as a function of electron dose (incident electron energy 500 eV). Each NO/NO_0 value was determined by XPS, with the NO_0 value measured prior to electron irradiation. Each $C_{ads}/C_{ads\ (e\text{-} = 1\times10^{18})}$ value was also determined by XPS and referenced to the value measured after an electron dose of 1×10^{18} e^-/cm^2. The *x* axis is shown on a log scale; the values at 1×10^{14} e^-/cm^2 correspond approximately to the electron dose experienced by the film prior to electron exposure, due to X-ray irradiation.

Figure 5a,b shows a comparison of the neutral gas phase species produced when (a) gas phase $Co(CO)_3NO$ molecules were exposed to 70 eV electrons in the quadrupole MS and (b) adsorbed $Co(CO)_3NO$ molecules were irradiated by 500 eV electrons. The fragmentation of gas phase $Co(CO)_3NO$ (Figure 5a) yields significant peaks for NO (m/z = 30), CO (m/z = 28), O (m/z = 16), and C (m/z = 12), with smaller contributions from Co (m/z = 58), CO_2 (m/z = 44 amu), and N (m/z = 14 amu). In contrast, Figure 5b represents an average of MS data taken every 20 s when a $Co(CO)_3NO$ film was exposed to 500 eV incident electrons for a total electron dose of 5×10^{16} e^-/cm^2. Analysis of Figure 5b reveals the presence of significant peaks for CO (m/z = 28 amu), O (m/z = 16 amu), and C (m/z = 12 amu), with smaller contributions from CO_2 (m/z = 44 amu), NO (m/z = 30 amu), and N (m/z = 14 amu). Figure 5b does not show any cobalt peak, corroborating the XPS data in Figures 1 and 2, which demonstrates that electron irradiation does not cause any cobalt to desorb from the surface (i.e., no electron stimulated $Co(CO)_3NO$ desorption).

Figure 6 shows how CO (m/z = 28 amu) production evolution and the coverage of surface bound NO species (NO/

dx.doi.org/10.1021/jp404905t | J. Phys. Chem. C 2013, 117, 16053−16064

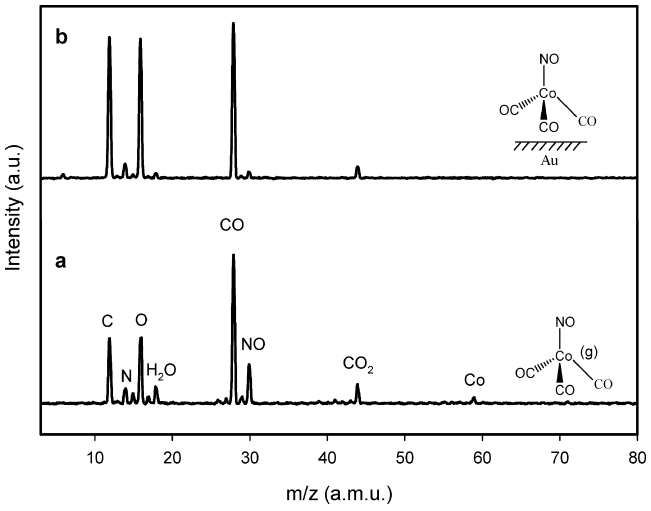

Figure 5. Mass spectrum (0–80 amu) of (a) gas phase $Co(CO)_3NO$ measured at $P_{Co(CO)_3NO} \approx 1.4 \times 10^{-7}$ Torr, (b) the volatile neutral species produced when a ~2.5 nm film of $Co(CO)_3NO$, adsorbed onto a gold substrate at −168 °C was irradiated by an electron dose of $5.00 \times 10^{+16}$ e^-/cm^2 (incident energy of 500 eV); the spectrum represents an average of MS taken every 20 s during the electron exposure.

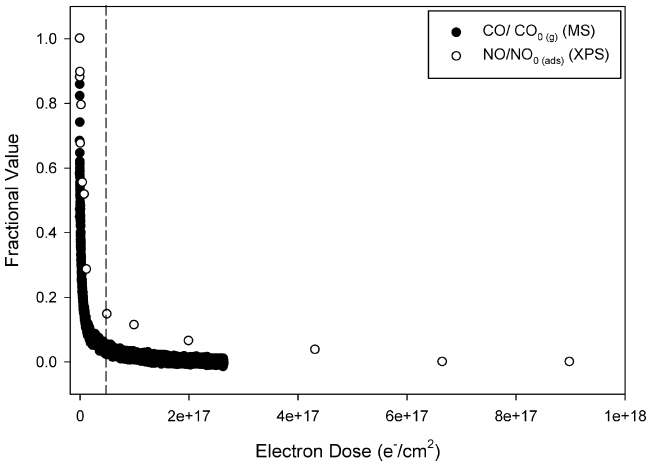

Figure 6. (Filled circles) Kinetics of gas phase CO (m/z = 28 amu) evolution from a $Co(CO)_3NO$ film and (open circles) fractional coverage of surface bound NO species (NO/NO_0). Both data sets were acquired for 2.3–2.5 nm $Co(CO)_3NO$ films as a function of electron dose (incident electron energy 500 eV). Vertical dotted line represents an electron dose of 5.00×10^{16} e^-/cm^2.

NO_0) species (also shown in Figure 4) vary as a function of electron dose. The kinetics of gas phase CO evolution and NO loss on the surface are seen to follow a similar dependence on electron dose, decreasing to 50% of their initial values for an electron dose of $\sim 8.00 \times 10^{15}$ e^-/cm^2.

Figure 7 shows the evolution in the C(1s), N(1s), O(1s), and $Co(2p_{3/2})$ regions for a 2.5 nm thick $Co(CO)_3NO$ film adsorbed onto a Au substrate at −168 °C, initially irradiated by an electron dose of 5×10^{16} e^-/cm^2, and then annealed to −29 °C, and then 25 °C. Upon electron irradiation, the same changes observed in Figure 1 are seen, notably that the two peaks in the C(1s) region decrease in intensity, the N(1s) region exhibits only the new nitride peak at 398.1 eV, the peaks in the O(1s) region decrease in intensity, while the $Co(2p_{3/2})$ region broadens slightly to higher binding energies. When this electron irradiated film is annealed from −168 to −29 °C there is no change in the C(1s), N(1s), O(1s) or $Co(2p_{3/2})$ regions. However, once the film is annealed to room temperature (25 °C) several changes are apparent. The nitride peak in the N(1s) region sharpens considerably while in the O(1s) region, the peaks associated with the CO and NO ligands decrease while the oxide peak at 529.7 eV increases in intensity. In the $Co(2p_{3/2})$ region there is a corresponding increase in the concentration of oxidized Co species. In the C(1s) region, all of the spectral intensity associated with CO species has gone when the substrate temperature reaches 25 °C, replaced by a small increase in the concentration of graphitic carbon. Indeed, the amount of carbon left on the surface at 25 °C is comparable to the level of carbon contamination present before $Co(CO)_3NO$ was dosed (spectra labeled "background" in the C(1s) region of Figure 7). In contrast, a significant amount of carbon remains for $Co(CO)_3NO$ films initially exposed to much larger electron doses (9×10^{17} e^-/cm^2) and then annealed to room temperature (uppermost spectra in the C(1s) region and labeled "9×10^{17}").

Figure 8 shows the evolution in the RAIR spectrum for a $Co(CO)_3NO$ film exposed to 500 eV electrons as a function of irradiation time. Prior to irradiation, this spectrum exhibits three peaks. The two higher frequency peaks, centered at 2111 cm^{-1} and 2064 cm^{-1} represent the symmetric (ν_s) and antisymmetric (ν_{as}) stretching modes of CO, respectively. The lower frequency peak centered at 1827 cm^{-1} corresponds to the NO stretching value. The two peaks in the CO stretching regions are very close to the gas phase values reported by Mcdowell et al., (2108 cm^{-1} (ν_s) and 2047 cm^{-1} (ν_{as}))[50] and these measured by Horrocks et al., (2100.3 cm^{-1} (ν_s) and 2033 cm^{-1} (ν_{as}))[51] when $Co(CO)_3NO$ was dissolved in cyclohexane. The peak position of the NO stretching mode also agrees with values reported for gas phase $Co(CO)_3NO$ (reported as being 1822 and 1806.2 cm^{-1}).[50,51] Prior to electron irradiation the adsorbed layer is therefore composed exclusively of molecular $Co(CO)_3NO$. As a function of increasing electron irradiation time, Figure 8 shows that all three peaks display a similar decrease in intensity, except for a slight shift to lower wavenumbers (1819 cm^{-1}) for the NO peak. For irradiation times in excess of 140 s the RAIR spectra are featureless. During electron irradiation no new IR features were observed in the remainder of the spectral window accessible to the MCT detector (400–4000 cm^{-1}).

Figure 9a,b shows the in situ AE spectra of a pyramidal EBID film deposited in the AES system in the presence of a constant partial pressure of $Co(CO)_3NO$ ($P_{Co(CO)_3NO} \approx 2.0 \times 10^{-7}$ Torr) onto an (a:C) substrate at room temperature (25 °C). Figure 9a,b shows that the EBID deposits are characterized primarily by Co (775, 716, and 656 eV) and O (503 eV) peaks with much smaller peaks associated with C (272 eV) and N (379 eV). The inset in Figure 9 shows an SEM image of a deposit.

DISCUSSION

In summary, our XPS data on surface transformations and corresponding MS data on evolved gas phase species, show that the purely electron stimulated reactions that occur to adsorbed $Co(CO)_3NO$ molecules can be partitioned into two steps. For electron doses $\leq 5 \times 10^{16}$ e^-/cm^2, the XPS data shows a significant decrease in the carbon and oxygen content

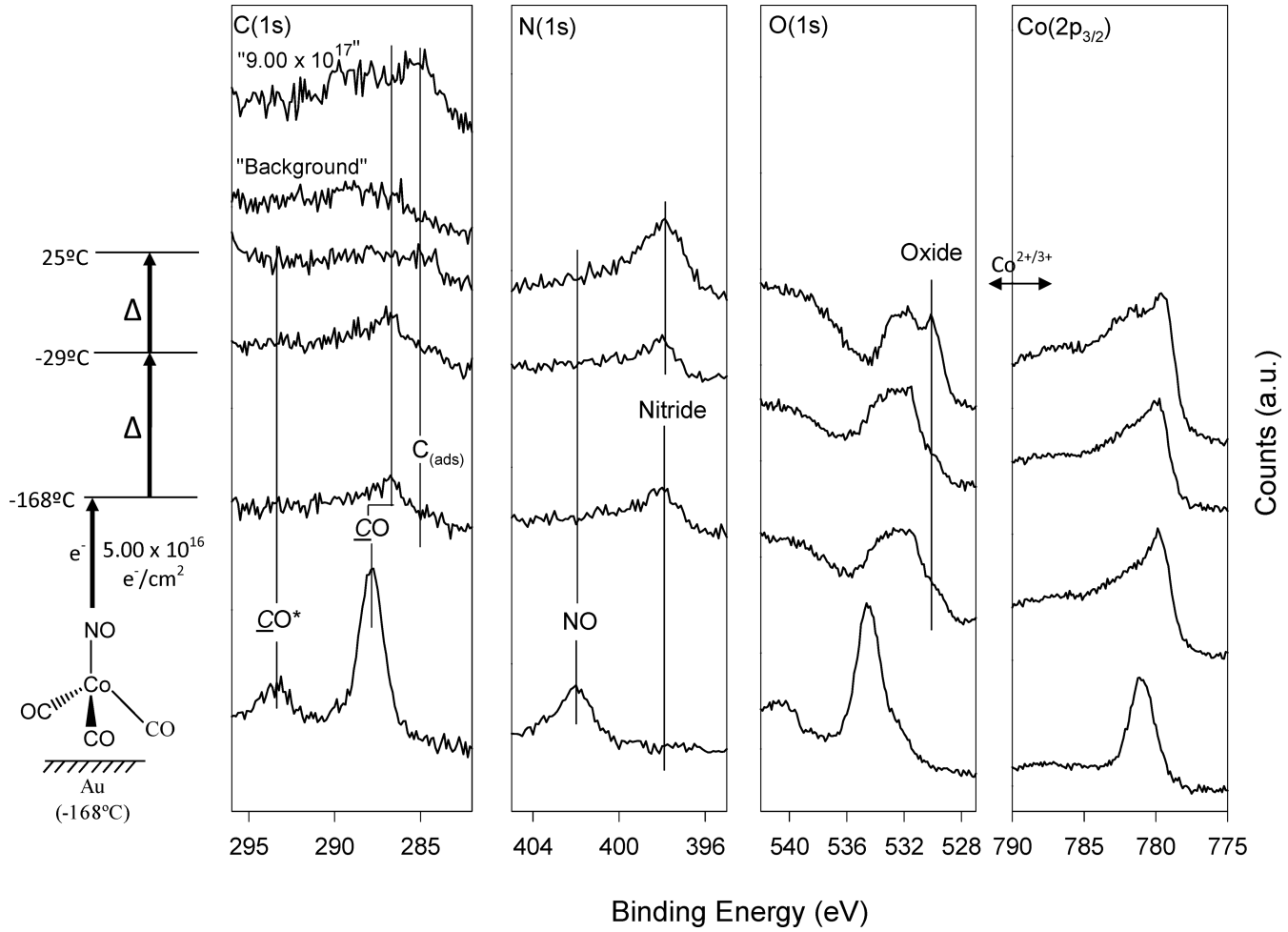

Figure 7. Effect of electron irradiation and then heating on the C(1s), N(1s), O(1s), and Co($2p_{3/2}$) XP regions for a ~2.5 nm thick film of $Co(CO)_3NO$ adsorbed onto a gold substrate. In the first step the film was irradiated by an electron dose of 5.0×10^{16} e^-/cm^2, at a substrate temperature of −168 °C. The electron irradiated film was then annealed in stages to 25 °C. Details of the uppermost two spectra in the C(1s) region labeled "background" and "9×10^{17}" can be found in the text.

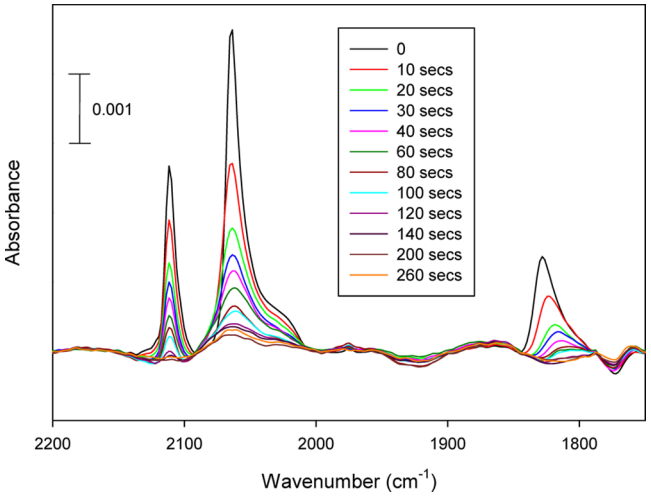

Figure 8. Effect of irradiation time (500 eV incident electrons) on the CO and NO stretching regions of a $Co(CO)_3NO$ film adsorbed onto a gold mirror at −168 °C. Each spectrum was ratioed to the clean gold mirror.

accompanied by a pronounced chemical transformation to the nitrogen atoms (Figures 1−3), while MS data shows a corresponding evolution of gas phase CO (Figures 5 and 6). In contrast, for electron doses >5×10^{16} e^-/cm^2 there is no more CO evolution and no more changes to the oxygen or carbon content in the film, although the spectroscopic signatures of adsorbed carbon and oxygen species continue to change (Figure 2). The overall reaction pathways elucidated by this study are summarized pictorially in Scheme 1.

In common with studies we have conducted on other organometallics,[38,39] the chemical identity of the substrate (Au or (a:C)) does not influence the sequence of electron stimulated reactions (compare Figures 1, 2, and Figure S2). This indicates that reactions are initiated within the adsorbate and are not influenced by any specific adsorbate−substrate interactions. In isolation our studies do not provide a definitive answer as to the relative role and importance of the primary 500 eV electrons and/or the low energy secondary electrons produced by the interactions of the primary beam with the substrate in initiating the reactions. However, the similar effects of X-ray irradiation (Figure S1) and the spectroscopic transformations shown in Figures 1 and 2 imply that it is the low energy secondary electrons that are most important. The IR data shown in Figure 8 demonstrates that $Co(CO)_3NO$ adsorbs molecularly at low temperatures, although there are no discernible spectroscopic changes as the film is irradiated except

dx.doi.org/10.1021/jp404905t | J. Phys. Chem. C 2013, 117, 16053−16064

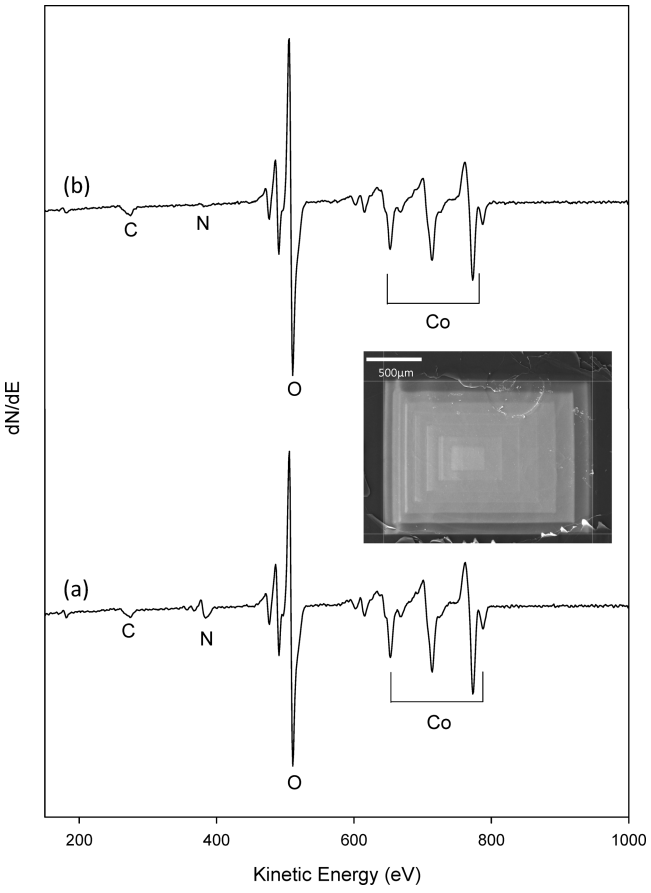

Figure 9. Auger electron spectra of EBID films created from $Co(CO)_3NO$ on an (a:C) substrate. Deposition conditions were $P_{Co(CO)_3NO} \approx 2.0 \times 10^{-7}$ Torr, incident beam energy = 3 keV, substrate current ~4.4 μA for a total electron dose of (a) 3.59×10^{28} e^-/cm^2 and (b) 3.08×10^{28} e^-/cm^2. Inset shows an SEM image of the deposit.

for the loss of the parent molecule. More detailed comparisons between IR and XPS/MS data are not warranted because of the unknown film thicknesses in IR experiments, which most likely correspond to thick multilayers, as compared to the <10 monolayer coverages used in XPS/MS experiments.

Step 1: Electron Stimulated CO Desorption and NO Decomposition. In this first step, which occurs for electron doses $\lesssim 5.00 \times 10^{16}$ e^-/cm^2, our XPS/MS data indicates that the overall chemical transformation can be represented as

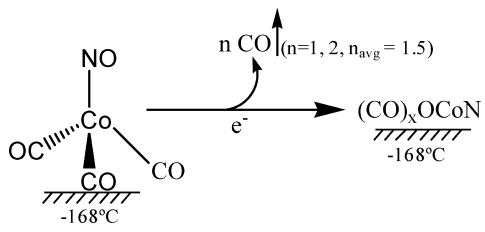

Direct experimental evidence for CO ejection from adsorbed $Co(CO)_3NO$ is provided by the mass spectrometry data in Figures 5 and 6, which show that CO rather than NO is the dominant gas phase species produced during electron irradiation, and that CO evolution occurs only during the initial stages of irradiation (i.e., for electron doses $\lesssim 5.00 \times 10^{16}$ e^-/cm^2). Consistent with the detection of gas phase CO, the XPS data in Figure 1 shows that for electron doses $\lesssim 5.00 \times 10^{16}$ e^-/cm^2 the dominant changes in the C(1s) and O(1s) regions involve a decrease in intensity of those spectroscopic features associated with the adsorbed CO ligands in the absence of any new spectroscopic features. Based on the ~50% decrease in the integrated C(1s) intensity (Figure 3), between one and two CO ligands are lost from adsorbed $Co(CO)_3NO$ molecules on average during this initial step. The ejection of a nonintegral number of CO ligands is a reflection of the propensity for metal carbonyls to lose multiple CO ligands in a statistical process as a consequence of electronic excitation/ionization. $(M(CO)_n + e^- \rightarrow M(CO)_{n-x}^{\pm} + xCO(g)\uparrow ; x = 1, 2, ..., n)$.[52−58] The loss of CO ligands also decomposes the metal carbonyl which causes the binding energy of the remaining CO species to decrease slightly (from 287.75 to 286.77 eV) and the satellite peak, observed in the C(1s) region, to disappear.

In marked contrast to the fate of CO ligands in this initial step, the NO ligand undergoes electron stimulated decomposition to produce a nitride species. This is clearly evidenced in Figure 1 by the appearance of a new peak in the N(1s) region at a significantly lower binding energy than the nitrogen species in the parent $Co(CO)_3NO$ molecules. Moreover, Figures 1 and 3 show that although the concentration of carbon atoms decreases by ~50% for electron doses $\lesssim 5.00 \times 10^{16}$ e^-/cm^2, the coverage of nitrogen atoms remains constant during this period, consistent with a decomposition process. Moreover, electron stimulated NO decomposition is seen to occur concurrently with CO desorption, evidenced most clearly in Figure 6 where the kinetics of NO loss measured on the surface, by XPS, mirrors the production of gas phase CO, as measured by mass spectrometry. Thus, the same molecular level transformation is responsible for CO ejection and NO decomposition. This preference for CO rather than NO ejection has also been observed in CVD reactions of $Co(CO)_3NO$ at elevated temperatures (>200 °C).[23]

After an electron dose of 5.00×10^{16} e^-/cm^2 a discernible oxide peak is observed within the O(1s) region in Figure 1 at a binding energy of 529.7 eV. At this stage of the reaction essentially all of the NO species in the parent $Co(CO)_3NO$ molecules have converted over to a nitride species but there is no evidence of any CO decomposition (i.e., step 1 has just been completed). Consequently, this oxide species must be a consequence of NO decomposition. Consistent with this assertion the $Co(2p_{3/2})$ region after an electron dose of 5.00×10^{16} e^-/cm^2 also shows the first tangible signs of broadening to higher binding energies due to the presence of oxidized cobalt atoms. It is also possible that during the decomposition step outlined in stage 1 some of the oxygen atoms in the nitrosyl ligands do not remain in the film and oxidizes cobalt atoms, but rather combine with CO ligands to produce the CO_2 that we observe in Figure 5, although the extent of this reaction is hard to gauge.

Step 1 represents the bond breaking process that converts the adsorbed molecular precursor $(Co(CO)_3NO_{(ads)})$ into a nonvolatile species that is now chemically bound to the substrate. This deposition event will occur as a result of electron interactions (either the incident primary beam or secondary electrons) with $Co(CO)_3NO_{(ads)}$, causing it to fragment. Figure S3 shows that the extent of reaction in step 1, as measured by the spectroscopic changes within the N(1s) region, is independent of the electron fluence and depends only on the electron dose, indicative of a one electron rate determining step. Our hypothesis is that step 1 occurs in a concerted manner where electronic excitation of the adsorbate is followed by the ejection of one or two CO ligands, creating a

dx.doi.org/10.1021/jp404905t | J. Phys. Chem. C 2013, 117, 16053−16064

short-lived intermediate that is unstable toward NO decomposition. The overall process can be represented as

$$Co(CO)_3NO(ads) + e^- \rightarrow [Co(CO)_3NO(ads)]^{+/-}$$

$$[Co(CO)_3NO(ads)]^{+/-} \rightarrow Co(CO)_xNO(ads) + (3 - x)CO\uparrow$$

$$Co(CO)_xNO(ads) \rightarrow (CO)_xOCoN(ads)$$

Under the steady state deposition conditions that describe EBID when it is performed in electron microscopes, the elementary reaction described by step 1 will occur after the precursor gas has been adsorbed onto the surface ($Co(CO)_3NO(g) \rightarrow Co(CO)_3NO(ads)$).

Step 2: Electron Stimulated Decomposition of Partially Decarbonylated $(CO)_xOCoN$ Species. The electron stimulated reactions in the first step transform the adsorbed cobalt tricarbonyl nitrosyl ($Co(CO)_3NO$) molecules into partially decarbonylated species where some of the CO ligands have desorbed and all of the NO ligands have decomposed. This species is referred to as $(CO)_xOCoN$, where x is 1 or 2. For electron doses >5.00×10^{16} e^-/cm^2, our experimental data indicate that further electron exposure causes these species to undergo electron stimulated CO decomposition.

$$(CO)_xOCoN \xrightarrow{e^-} (CoO_yN)C_{ads}$$
(-168°C) (-168°C)

Analysis of Figures 2−4 demonstrates that decomposition dominates for these larger electron doses, evidenced by the lack of change in the surface concentration of carbon, oxygen or nitrogen, while the adlayer continues to evolve, most notably via the production of adsorbed carbon, whose presence is only detected for electron doses in excess of ~5.0×10^{16} e^-/cm^2 (i.e., after the completion of step 1). Similarly, the MS data in Figure 6 shows that for electron doses in excess of ~5.00×10^{16} e^-/cm^2 the adsorbed layer no longer releases any CO. The concentration of oxide species and oxidized cobalt atoms also increases for these larger electron doses (Figure 2). Collectively, these observations point to a transformation of the CO ligands in the partially decarbonylated $(CO)_xOCoN$ species that can be represented as

$$CO(ads) + e^-C(ads) + O(\text{electron stimulated CO decomposition})$$

$$Co + O \rightarrow CoO(\text{oxidation of Co atoms})$$

This sequence of reaction steps is analogous to the behavior of CO ligands in partially decarbonylated species produced during the electron stimulated reactions of $W(CO)_6$.[39]

For electron doses in excess of ~9×10^{17} e^-/cm^2 the film's chemical composition remains constant, indicating that the reaction has reached completion. At this point the $Co(CO)_3NO$ molecules have been converted into a film that contains a mixture of metallic and oxidized cobalt atoms, nitrides and adsorbed carbon. The sequence of bond breaking steps described in steps 1 and 2 are summarized in Scheme 1.

A key goal of this work is to elucidate the elementary bond breaking steps that underpin the growth of nanostructures in typical EBID experiments, where deposition occurs on a substrate that is irradiated by an electron beam at ambient temperature in the presence of a constant partial pressure of precursor molecules. In contrast, the UHV experiments described, thus far, in the discussion section have addressed the electron induced transformations of $Co(CO)_3NO$ molecules adsorbed on solid substrates at low temperatures. In both

Scheme 1. Representation of the Electron and Thermally Stimulated Reactions of Adsorbed $Co(CO)_3NO$ Molecules

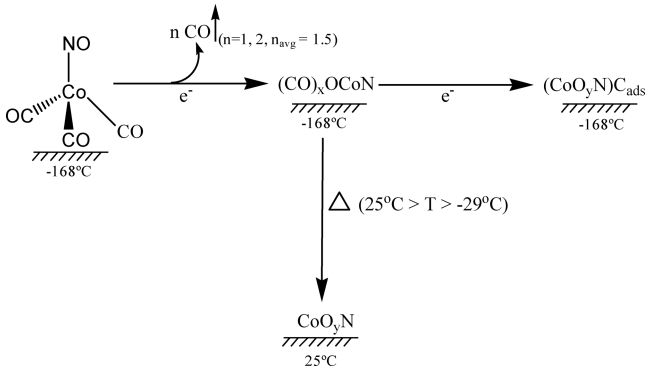

scenarios the initial step must be the same, specifically the electron stimulated bond-breaking step described in step 1 that converts the surface bound precursor molecules into adsorbed species. This is the step that allows EBID nanostructures to have their shapes and sizes determined so precisely by the incident electron beam. However, after this initial step a key difference emerges; notably that, in the UHV experiments, the residual fragments are bound at extremely low temperatures (−168 °C) where thermal processes will not contribute. In contrast, typical EBID experiments are conducted on substrates that are at ambient temperatures, where thermal reactions of the adsorbed species produced in the initial deposition step (step 1) could be important in determining the film's ultimate composition.

To address this issue, we conducted a number of experiments such as the one described in Figure 7 where $Co(CO)_3NO$ molecules were initially exposed to an electron dose of ~5×10^{16} e^-/cm^2, just enough to complete the initial deposition event described in step 1. These films were then annealed to room temperature as a means to determine the fate of the partially decarbonylated $(CO)_xOCoN$ species in typical (steady state) deposition situations. The most important finding of these experiments is seen in the C(1s) region of Figure 7 where the adsorbed CO species, and almost all of the carbon atoms have left the surface at room temperature. Indeed, a comparison of the C(1s) regions observed, (i) before dosing the precursor (labeled "background" in Figure 7) and (ii) after $Co(CO)_3NO$ was deposited, irradiated to an electron dose of 5×10^{16} e^-/cm^2 and then annealed to room temperature, are very similar to one another. The same lack of adsorbed carbon was observed for other $Co(CO)_3NO$ films that were exposed to electron doses <5×10^{16} e^-/cm^2 and then annealed to room temperature.

The significance of these observations is that they point to the thermal instability of the residual CO ligands in the partially decarbonylated $(CO)_xOCoN$ species created by the initial deposition step. Conversely, the nitride species formed during Step 1 are extremely stable to annealing and only disappear at substrate temperatures greater than 532 °C (data not shown). In terms of designing precursors that will yield EBID nanostructures with higher metal content, the use of nitrosyl (NO) ligands therefore seems to be compromised by their propensity for decomposition and the high thermal stability of the resultant nitride, although it does have the advantage of being carbon free.

Collectively, our experimental findings on the fate of the CO and NO ligands help to explain why EBID nanostructures

dx.doi.org/10.1021/jp404905t | J. Phys. Chem. C 2013, 117, 16053−16064

created from $Co(CO)_3NO$ under steady state deposition conditions, such as the ones used to create structures in our AES instrument and shown in Figure 9, typically contain nitrogen, but extremely low levels of carbon contamination.[18,19,29] This can be ascribed to the following sequence of bond breaking steps

$$Co(CO)_3NO(E) + e^- \rightarrow CoN(CO)_xO(ads)$$

electron stimulated deposition

$$CoN(CO)_xO\ (ads) + \Delta \rightarrow CoON(ads)$$

thermal reaction of the intermediate

Indeed, the level of nitrogen in EBID deposits created from $Co(CO)_3NO$ is usually greater than carbon.[18,19,29] For example, in the recent study by Gazzadi et al.[18] the atomic concentration of nitrogen in as-deposited EBID materials was ~50% greater than oxygen despite the fact that there are three times as many carbon atoms in the parent molecule. It should be noted, however that in the absence of thermally accessible reaction channels the CO ligands in the intermediate $(CO)_xOCoN$ (ads) will undergo electron stimulated decomposition, as described in step 2

$$CoN(CO)_xO(ads) + e^- \rightarrow (CoO_yN)C(ads)$$

The adsorbed carbon atoms (C_{ads}) produced in this step are graphite like and remain stable at RT. This is shown explicitly in the uppermost spectra in the C(1s) region of Figure 7 (labeled "9×10^{17}") where a large amount of adsorbed carbon is seen to remain on the surface when a $Co(CO)_3NO$ film was exposed to an electron dose of 9.00×10^{17} e^-/cm^2, sufficient to decompose all of the CO ligands in the $(CO)_xOCoN$ intermediate (see Figure 2), and then annealed to room temperature.

In typical EBID experiments the fate of the $(CO)_xOCoN$ (ads) intermediates produced as a consequence of the initial deposition event that causes CO ligands to be ejected and the NO ligand to dissociate (step 1), can be viewed as a competition between electron and thermal stimulated processes, with the thermal channel being preferred from the point of view of improving metal content in the deposits. On the basis of this idea of competitive partitioning, shown pictorially in Scheme 1, we would predict that the carbon content in EBID deposits created from $Co(CO)_3NO$ would decrease as the substrate temperature increases, due to the increased rate and therefore importance of the thermal reaction that favors carbon loss. This trend has been observed in a recent study by Mulders et al., who studied changes in composition and purity of EBID structures created from $Co(CO)_3NO$ at different substrate temperatures.[29] Indeed, for substrate temperatures >50 °C, oxygen and nitrogen were the only organic species observed in the deposits.[29] In a broader sense, results from this study reinforce the key finding of previous studies on EBID precursors, such as $Pt(PF_3)_4$, $W(CO)_6$, and $MeCpPt(Me)_3$, notably that electron stimulated deposition followed by thermal reactions of the residual ligands produce deposits with greater metal purity compared to situations where the precursors were decomposed exclusively by electron beam irradiation.[40]

Results from the present investigation can also be compared to recent gas phase studies of $Co(CO)_3NO$ interactions with the low energy electrons (<10 eV) that are widely believed to play a determinant role in EBID.[33,34] Since gas phase studies probe the interactions of electrons with the parent molecule they are restricted to providing information that relates to the initial bond-breaking step (i.e., step 1). For $Co(CO)_3NO$, a comparison of these previous gas phase studies and the present UHV surface science study reveals important differences and similarities. Both studies indicate a propensity for CO rather than NO desorption. Based on the analysis of Engmann et al., this selectivity in bond breaking supports the idea that the reactions are initiated by very low energy electrons (<1 eV), because CO ejection from $[Co(CO)_3NO]^-$ is exothermic with an electron energy threshold of ~−0.3 eV, whereas NO release is slightly endothermic with an energy threshold of ~0.2 eV.[34] This difference can be traced back to the differences in Co−CO and Co−NO binding energies (Co−CO ≈ 1.42 eV compared to Co−NO ≈ 1.70 eV).[59] The gas phase studies also show that the cross-section for CO ejection from $Co(CO)_3NO$ is an order of magnitude greater than for NO.[34] However, there is no suggestion from the gas phase studies that CO desorption is accompanied by NO decomposition, which is clearly evident for the adsorbed molecule. We suspect that this difference is a reflection of the fact that in the present study CO desorption creates a partially decarbonylated species bound to the substrate where the charge has been dissipated, while in the gas phase isolated anions such as $[Co(CO)_2NO]^-$ are created,[34] from which NO decomposition would seem to be far less likely. The extent of CO desorption is also somewhat greater for the adsorbed molecules with an average of between one and two CO ligands being lost in the initial electron-molecule interaction, while the gas phase studies show a distinct preference for the loss of only one CO ligand.[34]

The recent gas phase $Co(CO)_3NO$ work of Engmann et al., also showed that although partially decarbonylated species were the dominant product of low energy (<10 eV) interactions with gas phase $Co(CO)_3NO$, the reactions of higher energy electrons (>70 eV) led to the formation of bare Co atoms as the major product.[34] Consequently, the extent to which these two electron stimulated processes contribute to EBID in the case of $Co(CO)_3NO$ could be determined by monitoring the chemical composition of deposits formed as the incident electron energy is varied between zero and several thousand eV.

CONCLUSIONS

The initial deposition step in the electron stimulated reactions of surface bound cobalt tricarbonyl nitrosyl ($Co(CO)_3NO$) occurs through a one electron process that is characterized by the loss of carbon and oxygen atoms from the film through the ejection of one or two CO ligands and the transformation of the adsorbed nitrogen atoms due to cleavage of the N≡O bonds. Collectively, these two processes yield a partially decarbonylated cobalt-containing intermediate where nitride species are also present. In traditional EBID experiments conducted in electron microscopes the fate of this intermediate will depend on the details of the deposition conditions. At low substrate temperatures electron stimulated decomposition of the residual CO ligands will be important, leading to the accumulation of carbon in the deposit. However, at higher substrate temperatures thermal reactions that result in carbon loss from the intermediate become dominant, causing a corresponding increase in the metal content. Based on the mechanistic insights uncovered in this study the propensity for $Co(CO)_3NO$ to create EBID nanostructures with low levels of carbon contamination compared to most organometallic precursors is ascribed to the thermal instability of the Co−

CO bonds in the partially decarbonylated intermediates formed in the initial deposition step.

■ ASSOCIATED CONTENT

Supporting Information

Data on the effect of (**S1**) X-ray irradiation on adsorbed $Co(CO)_3NO$ molecules; (**S2**) electron irradiation on $Co(CO)_3NO$ molecules adsorbed onto (a:C) rather than substrates; (**S3**) electron fluence on the extent of nitrogen decomposition. This material is available free of charge via the Internet at http://pubs.acs.org.

■ AUTHOR INFORMATION

Corresponding Author

*E-mail: howardf@jhu.edu.

Notes

The authors declare no competing financial interest.

■ REFERENCES

(1) van Dorp, W. F.; Hagen, C. W., A Critical Literature Review of Focused Electron Beam Induced Deposition. *J. Appl. Phys.* **2008**, *104*.
(2) Utke, I.; Hoffmann, P.; Melngailis, J. Gas-Assisted Focused Electron Beam and Ion Beam Processing and Fabrication. *J. Vac. Sci. Technol. B* **2008**, *26*, 1197−1276.
(3) Randolph, S. J.; Fowlkes, J. D.; Rack, P. D. Focused, Nanoscale Electron-Beam-Induced Deposition and Etching. *Crit Rev. Solid State* **2006**, *31*, 55−89.
(4) Silvis-Cividjian, N.; Hagen, C. W.; Kruit, P.; Van der Stam, M. A. J.; Groen, H. B. Direct Fabrication of Nanowires in an Electron Microscope. *Appl. Phys. Lett.* **2003**, *82*, 3514−3516.
(5) Huth, M.; Porrati, F.; Schwalb, C.; Winhold, M.; Sachser, R.; Dukic, M.; Adams, J.; Fantner, G. Focused Electron Beam Induced Deposition: A Perspective. *Beilstein J. Nanotechnol.* **2012**, *3*, 597−619.
(6) Fernandez-Pacheco, A.; De Teresa, J. M.; Cordoba, R.; Ibarra, M. R., Magnetotransport Properties of High-Quality Cobalt Nanowires Grown by Focused-Electron-Beam-Induced Deposition. *J. Phys. D Appl. Phys.* **2009**, *42*.
(7) Gabureac, M.; Bernau, L.; Utke, I.; Boero, G., Granular Co-C Nano-Hall Sensors by Focused-Beam-Induced Deposition. *Nanotechnology* **2010**, *21*.
(8) Fernandez-Pacheco, A.; De Teresa, J. M.; Cordoba, R.; Ibarra, M. R.; Petit, D.; Read, D. E.; O'Brien, L.; Lewis, E. R.; Zeng, H. T.; Cowburn, R. P., Domain Wall Conduit Behavior in Cobalt Nanowires Grown by Focused Electron Beam Induced Deposition. *Appl. Phys. Lett.* **2009**, *94*.
(9) Lavrijsen, R.; Lee, J. H.; Fernandez-Pacheco, A.; Petit, D. C. M. C.; Mansell, R.; Cowburn, R. P. Magnetic Ratchet for Three-Dimensional Spintronic Memory and Logic. *Nature* **2013**, *493*, 647−650.
(10) Nikulina, E.; Idigoras, O.; Vavassori, P.; Chuvilin, A.; Berger, A. Magneto-Optical Magnetometry of Individual 30 nm Cobalt Nanowires Grown by Electron Beam Induced Deposition. *Appl. Phys. Lett.* **2012**, *100*, 142401/142401−142401/142404.
(11) Rodriguez, L. A.; Magen, C.; Snoeck, E.; Serrano-Ramon, L.; Gatel, C.; Cordoba, R.; Martinez-Vecino, E.; Torres, L.; De Teresa, J. M.; Ibarra, M. R. Optimized Cobalt Nanowires for Domain Wall Manipulation Imaged by in Situ Lorentz Microscopy. *Appl. Phys. Lett.* **2013**, *102*, 2.
(12) Botman, A.; de Winter, D. A. M.; Mulders, J. J. L. Electron-Beam-Induced Deposition of Platinum at Low Landing Energies. *J. Vac. Sci. Technol. B* **2008**, *26*, 2460−2463.
(13) Botman, A.; Hesselberth, M.; Mulders, J. J. L. Improving the Conductivity of Platinum-Containing Nano-Structures Created by Electron-Beam-Induced Deposition. *Microelectron. Eng.* **2008**, *85*, 1139−1142.
(14) Botman, A.; Mulders, J. J. L.; Weemaes, R.; Mentink, S. Purification of Platinum and Gold Structures after Electron-Beam-Induced Deposition. *Nanotechnology* **2006**, *17*, 3779−3785.
(15) Koops, H. W. P.; Kaya, A.; Weber, M. Fabrication and Characterization of Platinum Nanocrystalline Material Grown by Electron-Beam Induced Deposition. *J. Vac. Sc.i Technol. B* **1995**, *13*, 2400−2403.
(16) Utke, I.; Hoffmann, P.; Berger, R.; Scandella, L. High-Resolution Magnetic Co Supertips Grown by a Focused Electron Beam. *Appl. Phys. Lett.* **2002**, *80*, 4792−4794.
(17) Lau, Y. M.; Chee, P. C.; Thong, J. T. L.; Ng, V. Properties and Applications of Cobalt-Based Material Produced by Electron-Beam-Induced Deposition. *J. Vac. Sci. Technol. A* **2002**, *20*, 1295−1302.
(18) Gazzadi, G. C.; Mulders, H.; Trompenaars, P.; Ghirri, A.; Affronte, M.; Grillo, V.; Frabboni, S. Focused Electron Beam Deposition of Nanowires from Cobalt Tricarbonyl Nitrosyl ($Co(CO)_3NO$) Precursor. *J. Phys. Chem. C* **2011**, *115*, 19606−19611.
(19) Gazzadi, G. C.; Mulders, J. J. L.; Trompenaars, P.; Ghirri, A.; Rota, A.; Affronte, M.; Frabboni, S. Characterization of a New Cobalt Precursor for Focused Beam Deposition of Magnetic Nanostructures. *Microelectron. Eng.* **2011**, *88*, 1955−1958.
(20) Ervin, M. H.; Nichols, B. M. Electron Beam Induced Deposition of Cobalt for Use as Single- and Multiwalled Carbon Nanotube Growth Catalyst. *J. Vac. Sci. Technol., B* **2009**, *27*, 2982−2985.
(21) Fernandez-Pacheco, A.; De Teresa, J. M.; Cordoba, R.; Ibarra, M. R. Magnetotransport Properties of High-Quality Cobalt Nanowires Grown by Focused-Electron-Beam-Induced Deposition. *J. Phys. D: Appl. Phys.* **2009**, *42*, 055005.
(22) Boero, G.; Utke, I.; Bret, T.; Quack, N.; Todorova, M.; Mouaziz, S.; Kejik, P.; Brugger, J.; Popovic, R. S.; Hoffmann, P., Submicrometer Hall Devices Fabricated by Focused Electron-Beam-Induced Deposition. *Appl. Phys. Lett.* **2005**, *86*.
(23) Ivanova, A. R.; Nuesca, G.; Chen, X. M.; Goldberg, C.; Kaloyeros, A. E.; Arkles, B.; Sullivan, J. J. The Effects of Processing Parameters in the Chemical Vapor Deposition of Cobalt from Cobalt Tricarbonyl Nitrosyl. *J. Electrochem. Soc.* **1999**, *146*, 2139−2145.
(24) Choi, S. W. K.; Puddephatt, R. J. Cobalt-Palladium and Cobalt-Platinum Bilayer Films Formed by Chemical Vapor Deposition. *Chem. Mater.* **1997**, *9*, 1191−1195.
(25) Maruyama, T.; Nakai, T. Cobalt Oxide Thin-Films Prepared by Chemical Vapor-Deposition from Cobalt(II) Acetate. *Sol. Energ. Mater.* **1991**, *23*, 25−29.
(26) Maruyama, T.; Nakai, T. Cobalt Thin-Films Prepared by Chemical Vapor-Deposition from Cobaltous Acetate. *Appl. Phys. Lett.* **1991**, *59*, 1433−1434.
(27) Frabboni, S.; Gazzadi, G. C.; Spessot, A. Tem Study of Annealed Pt Nanostructures Grown by Electron Beam-Induced Deposition. *Physica E* **2007**, *37*, 265−269.
(28) Folch, A.; Servat, J.; Esteve, J.; Tejada, J.; Seco, M. High-Vacuum Versus "Environmental" Electron Beam Deposition. *J. Vac. Sci. Technol. B* **1996**, *14*, 2609−2614.
(29) Mulders, J. J. L.; Belova, L. M.; Riazanova, A. Electron Beam Induced Deposition at Elevated Temperatures: Compositional Changes and Purity Improvement. *Nanotechnology* **2011**, *22*, 055302/055301−055302/055307.
(30) Cicoira, F.; Leifer, K.; Hoffmann, P.; Utke, I.; Dwir, B.; Laub, D.; Buffat, P. A.; Kapon, E.; Doppelt, P. Electron Beam Induced Deposition of Rhodium from the Precursor $[RhCl(PF_3)_2]_2$: Morphology, Structure and Chemical Composition. *J. Cryst. Growth* **2004**, *265*, 619−626.
(31) Luisier, A.; Utke, I.; Bret, T.; Cicoira, F.; Hauert, R.; Rhee, S. W.; Doppelt, P.; Hoffmann, P. Comparative Study of Cu-Precursors for 3d Focused Electron Beam Induced Deposition. *J. Electrochem. Soc.* **2004**, *151*, C590−C593.
(32) Gazzadi, G. C.; Frabboni, S.; Menozzi, C., Suspended Nanostructures Grown by Electron Beam-Induced Deposition of Pt and Teos Precursors. *Nanotechnology* **2007**, *18*.
(33) Engmann, S.; Stano, M.; Matejcik, S.; Ingolfsson, O. The Role of Dissociative Electron Attachment in Focused Electron Beam Induced

Processing: A Case Study on Cobalt Tricarbonyl Nitrosyl. *Angew. Chem., Int. Ed.* **2011**, *50*, 9475−9477.
(34) Engmann, S.; Stano, M.; Papp, P.; Brunger, M. J.; Matejcik, S.; Ingolfsson, O. Absolute Cross Sections for Dissociative Electron Attachment and Dissociative Ionization of Cobalt Tricarbonyl Nitrosyl in the Energy Range from 0 to 140 eV. *J. Chem. Phys.* **2013**, *138*, 044305/044301−044305/044307.
(35) Schaefer, J.; Hoelzl, J. Contribution to Dependence of Secondary-Electron Emission from Work Function and Fermi Energy. *Thin Solid Films* **1972**, *13*, 81−&.
(36) Wnuk, J. D.; Gorham, J. M.; Rosenberg, S. G.; van Dorp, W. F.; Madey, T. E.; Hagen, C. W.; Fairbrother, D. H. Electron Induced Surface Reactions of the Organometallic Precursor Trimethyl-(Methylcyclopentadienyl)Platinum(IV). *J. Phys. Chem. C* **2009**, *113*, 2487−2496.
(37) Wnuk, J. D.; Gorham, J. M.; Rosenberg, S. G.; van Dorp, W. F.; Madey, T. E.; Hagen, C. W.; Fairbrother, D. H., Electron Beam Irradiation of Dimethyl-(Acetylacetonate) Gold(III) Adsorbed onto Solid Substrates. *J. Appl. Phys.* **2010**, *107*.
(38) Landheer, K.; Rosenberg, S. G.; Bernau, L.; Swiderek, P.; Utke, I.; Hagen, C. W.; Fairbrother, D. H. Low-Energy Electron-Induced Decomposition and Reactions of Adsorbed Tetrakis-(Trifluorophosphine)Platinum [$Pt(PF_3)_4$]. *J. Phys. Chem. C* **2011**, *115*, 17452−17463.
(39) Rosenberg, S. G.; Barclay, M.; Fairbrother, D. H. Electron Induced Reactions of Surface Adsorbed Tungsten Hexacarbonyl ($W(CO)_6$). *Phys. Chem. Chem. Phys.* **2013**, *15*, 4002−4015.
(40) Rosenberg, S. G.; Landheer, K.; Hagen, C. W. Substrate Temperature and Electron Fluence Effects on Metallic Films Created by Electron Beam Induced Deposition. *J. Vac. Sci. Technol. B* **2012**, *30*, 051805.
(41) Tanuma, S.; Powell, C. J.; Penn, D. R. Calculations of Electron Inelastic Mean Free Paths. *Surf. Interface Anal.* **1991**, *17*, 911−926.
(42) Moulder, J. F., et al., *Handbook of X-Ray Photoelectron Spectroscopy*. Physical Electronics USA, Inc.: Chanhassen: 1995.
(43) Plummer, E. W.; Salaneck, W. R.; Miller, J. S. Photoelectron-Spectra of Transition-Metal Carbonyl-Complexes - Comparison with Spectra of Adsorbed Co. *Phys. Rev. B* **1978**, *18*, 1673−1701.
(44) Barber, M.; Connor, J. A.; Guest, M. F.; Hall, M. B.; Hillier, I. H.; Meredith, W. N. High-Energy Photoelectron Spectroscopy of Transition-Metal Complexes 0.1. Bonding in Substituted and Unsubstituted First Row Carbonyls. *Faraday Discuss* **1972**, *54*, 219−226.
(45) Wagner, A. J.; Wolfe, G. M.; Fairbrother, D. H. Reactivity of Vapor-Deposited Metal Atoms with Nitrogen-Containing Polymers and Organic Surfaces Studied by in Situ Xps. *Appl. Surf. Sci.* **2003**, *219*, 317−328.
(46) Bertoti, I. Characterization of Nitride Coatings by XPS. *Surf. Coat. Technol.* **2002**, *151*, 194−203.
(47) Chuang, T. J.; Brundle, C. R.; Rice, D. W. Interpretation of the X-Ray Photoemission Spectra of Cobalt Oxides and Cobalt Oxide Surfaces. *Surf. Sci.* **1976**, *59*, 413−429.
(48) Christoskova, S.; Stoyanova, M.; Georgieva, M.; Mehandjiev, D. Preparation and Characterization of a Higher Cobalt Oxide. *Mater. Chem. Phys.* **1999**, *60*, 39−43.
(49) Barreca, D.; Massignan, C.; Daolio, S.; Fabrizio, M.; Piccirillo, C.; Armelao, L.; Tondello, E. Composition and Microstructure of Cobalt Oxide Thin Films Obtained from a Novel Cobalt(II) Precursor by Chemical Vapor Deposition. *Chem. Mater.* **2001**, *13*, 588−593.
(50) Mcdowell, R. S.; Horrocks, W. D.; Yates, J. T. Infrared Spectrum of $Co(CO)_3NO$. *J. Chem. Phys.* **1961**, *34*, 530−534.
(51) Horrocks, W. D.; Taylor, R. C. Infrared Spectroscopic Study of Derivatives of Cobalt Tricarbonyl Nitrosyl. *Inorg. Chem.* **1963**, *2*, 723−727.
(52) Bidinosti, D. R.; McIntyre, N. S. Electron-Impact Study of Some Binary and Metal Carbonyls. *Can. J. Chem.* **1967**, *45*, 641−648.
(53) Foffani, A.; Cantone, B.; Pignataro, S.; Grasso, F. Mass Spectra of Metal Hexacarbonyls. *Zeitschrift Fur Physikalische Chemie-Frankfurt* **1965**, *45*, 79−88.
(54) Pignataro, S.; Foffani, A.; Grasso, F.; Cantone, B. Negative Ions from Metal Carbonyls by Electron Impact. *Zeitschrift Fur Physikalische Chemie-Frankfurt* **1963**, *47*, 106−113.
(55) Qi, F.; Yang, S. H.; Sheng, L. S.; Gao, H.; Zhang, Y. W.; Yu, S. Q. Vacuum Ultraviolet Photoionization and Dissociative Photoionization of $W(CO)_6$. *J. Chem. Phys.* **1997**, *107*, 10391−10398.
(56) Winters, R. E.; Kiser, R. W. Mass Spectrometric Studies of Chromium Molybdenum and Tungsten Hexacarbonyls. *Inorg. Chem.* **1965**, *4*, 157−161.
(57) Wnorowski, K.; Stano, M.; Barszczewska, W.; Jówko, A.; Matejčík, Š. Electron Ionization of $W(CO)_6$: Appearance Energies. *Int. J. Mass Spectrom.* **2012**, *314*, 42−48.
(58) Wnorowski, K.; Stano, M.; Matias, C.; Denifl, S.; Barszczewska, W.; Matejčík, Š. Low-Energy Electron Interactions with Tungsten Hexacarbonyl - $W(CO)_6$. *Rapid Commun. Mass Spectrom.* **2012**, *26*, 1−6.
(59) Opitz, J. Electron Impact Ionization of Cobalt-Tricarbonyl-Nitrosyl, Cyclopentadienyl-Cobalt-Dicarbonyl and Biscyclopentadienyl-Cobalt: Appearance Energies, Bond Energies and Enthalpies of Formation. *Int. J. Mass Spectrom.* **2003**, *225*, 115−126.